

Dynamic Symmetry Breaking and Spin Splitting in Metal Halide Perovskites

Scott McKechnie,¹ Jarvist M. Frost,² Dimitar Pashov,¹ Pooya Azarhoosh,¹ Aron Walsh*,^{2,3} and Mark van Schilfgaarde*¹

¹Department of Physics, King's College London, London WC2R 2LS, UK

²Department of Materials, Imperial College London, London SW7 2BZ, UK

³Department of Materials Science and Engineering, Yonsei University, Seoul 03722, Korea*

(Dated: February 15, 2022)

Metal halide perovskites exhibit a materials physics that is distinct from traditional inorganic and organic semiconductors. While materials such as $\text{CH}_3\text{NH}_3\text{PbI}_3$ are non-magnetic, the presence of heavy elements (Pb and I) in a non-centrosymmetric crystal environment result in a significant spin-splitting of the frontier electronic bands through the Rashba-Dresselhaus effect. We show, from a combination of *ab initio* molecular dynamics, density-functional theory, and relativistic quasi-particle *GW* theory, that the nature (magnitude and orientation) of the band splitting depends on the local asymmetry around the Pb and I sites in the perovskite structure. The potential fluctuations vary in time as a result of thermal disorder and a dynamic lone pair instability of the $\text{Pb(II)}\ 6s^26p^0$ ion. We show that the same physics emerges both for the organic-inorganic $\text{CH}_3\text{NH}_3\text{PbI}_3$ and the inorganic CsPbI_3 compound. The results are relevant to the photophysics of these compounds and are expected to be general to other lead iodide containing perovskites.

In crystals that preserve both time-reversal and spatial-inversion symmetry, there is at least a double degeneracy of the electron energy bands $E_n(k)$ for each wave vector k in the Brillouin zone [1]. However, the removal of spatial inversion symmetry produces an asymmetric potential, which, through the spin-orbit interaction, lifts the two-fold spin degeneracy [2]. Dresselhaus and Rashba were the first to provide group theory descriptions of the effect of spin-orbit coupling (SOC) on non-centrosymmetric zincblende [3] and wurtzite [4–6] structures [7]. In a later work, Bychkov and Rashba pointed out that the analysis also applied to 2D systems [8]. The so-called Rashba effect is associated with a spin splitting of the dispersion $E(k)$ that is linear in k and a spin texture that is helical [2, 5, 9]. On the other hand, the Dresselhaus effect typically displays a splitting that is cubic in k and a nonhelical spin texture [2, 3, 9]. A recent study by Zunger et al. [10], provides a concise definition of the Rashba and Dresselhaus spin splittings, emphasising the local origin of these effects: atomic sites without inversion symmetry can either be polar (local Rashba) or nonpolar (local Dresselhaus) and the bulk effect is a vector sum over all sites (allowing for the coexistence of bulk Rashba and bulk Dresselhaus). Both are rooted in spin-orbit interactions at sites with local asymmetry and result in spin-split bands; from here on, ‘spin splitting’ will be used as a collective term for the two effects.

Spin splitting is now seen as a crucial feature in the electronic structure of solid-state systems. Indeed, exploiting these effects to control the electron spin is a central goal in spintronics [11, 12]. It is also emerging as an important aspect of materials for photovoltaics, where it is thought to strongly influence the absorption and transport properties in perovskite solar cells [13–25]. Metal halide perovskites have attracted significant attention for solar-energy conversion, with champion light-to-electricity conversion efficiencies exceeding 22 % for laboratory scale devices [26, 27]. The unique chemistry and physics of these materials is also extending their range of applications to areas including light-emitting diodes, spintronics, solid-state memory and solid-state sensors [28, 29].

The archetype material, $\text{CH}_3\text{NH}_3\text{PbI}_3$ (or MAPbI_3), is composed of corner-sharing lead-iodide octahedra, with a charge-balancing organic cation in the void regions, forming a three-dimensional perovskite structure. With the large nuclear charges of lead and iodine, the electron kinetic energies near these cores are large. Relativistic effects become important. These materials also exhibit reduced symmetry (both static and dynamic) resulting in local asymmetry which, through the Rashba and Dresselhaus effects, can split the bands into separate spin channels and shift the location of valence and conduction band extrema. This can lead to spin and momentum forbidden transitions that suppress electron-hole recombination [16, 18, 30]. First-principles electronic-structure calculations predicted that such relativistic effects could result in a direct to indirect bandgap transition in Pb-based perovskites [13–18]. There are increasing data to support this hypothesis. Indirect transitions are implicated for the observed slow minority carrier recombination [22–25]. In particular, angle-resolved X-ray photoemission spectroscopy (ARPES) has been used to directly resolve indirect features in the band structure [23].

In this Letter, we study the effect of local symmetry breaking (arising both statically and dynamically) on the electronic structure of lead halide perovskites. We sample structures from finite-temperature molecular dynamic simulations and evaluate the spin splitting. The band splitting directly impacts the photophysics of an operating solar cell, and it is also a relevant metric of local asymmetry. By making identical studies of both organic-cation and inorganic perovskites, we show that similar behaviour is present. Both organic and inorganic finite-temperature structures exhibit significant band splitting. The soft polar nature of halide perovskites leads to large distortions and resulting asymmetry at heavy atom sites. With Pb-based perovskites, this leads to particularly pronounced spin splittings. We correlate a metric relevant for device physics (spin-split bands) directly with features that can be observed (lattice distortion).

The electronic structure of lead halide perovskites is sen-

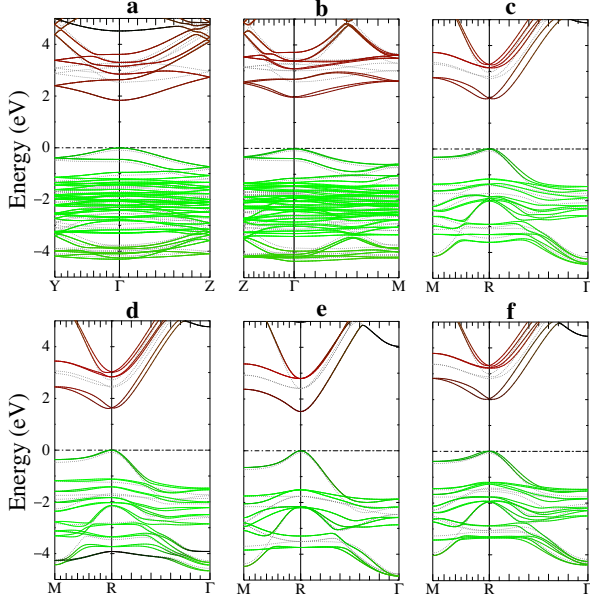


FIG. 1: Relativistic QSGW electronic band structures. $\text{CH}_3\text{NH}_3\text{PbI}_3$ in its (a) orthorhombic, (b) tetragonal and (c) pseudocubic phases. $\text{HC}(\text{NH}_2)_2\text{PbI}_3$ in a (d) pseudocubic structure and CsPbI_3 in (e) cubic and (f) pseudocubic structures. The pseudocubic CsPbI_3 is obtained by substituting Cs into $\text{CH}_3\text{NH}_3\text{PbI}_3$. Bands are coloured based on a Mulliken projection: Pb p states are highlighted in red and I p states in green.

sitive to the choice of Hamiltonian [31, 32]. Relativistic effects lower and split the atomic levels of Pb and I (Table S1). These effects carry over into the condensed phase, resulting in a large renormalization of the bandgap (Table I). There is in addition, a k -dependent contribution originating from local asymmetry and spin-orbit coupling, which gives rise to the aforementioned spin splitting. As a result, the inclusion of scalar-relativistic and SOC corrections is essential for a correct description of the band structure [13, 32]. In these materials, the quasi-particle corrections are large, which necessitates going beyond Kohn-Sham density-functional theory (DFT) [13, 33, 34]. Here we use relativistic quasi-particle GW theory (QSGW), as implemented in the all-electron QUESTAAL [35] software package. For its greater computational efficiency, we also use the local density approximation (LDA) [36] to calculate the electronic structure of structures sampled from molecular dynamics (MD) trajectories, and a set of structures sampled from lattice dynamics. These we reference against QSGW calculations on individual cases. Further computational details are provided as Supplemental Material.

Static crystal structure representations. As an initial reference we study static geometry-relaxed crystal structures. Our calculated QSGW band structures of $\text{CH}_3\text{NH}_3\text{PbI}_3$ in three phases are shown in Fig. 1. These structures have been carefully energy-minimized for lattice dynamics calculations [37]. The low-temperature orthorhombic (D_{2h} point group)

TABLE I: Bandgaps (E_g) and conduction band splittings (ΔE and Δk) for a range of halide perovskites calculated for static (athermal) structures using QSGW including scalar-relativistic effects, and spin-orbit coupling (SOC) where stated. Measured bandgaps, E_g^{EXP} , are also shown.

Material	E_g (eV)	E_g^{SOC}	E_g^{EXP}	ΔE (meV)	Δk (\AA^{-1})
o-MAPbI ₃	2.63	1.84	1.65 [39]	0	0
t-MAPbI ₃	2.67	1.99	1.61 [39]	10	0.03
pc-MAPbI ₃	2.72	1.87	1.63 [40]	82	0.06
pc-FAPbI ₃	2.52	1.61	1.52 [39]	24	0.03
pc-CsPbI ₃	2.81	1.95		82	0.06
c-CsPbI ₃	2.48	1.51	1.73 [41]	0	0

phase has a conventional-looking band structure with a direct bandgap. The principal effect of SOC (compare dashed grey and colored lines) is a large renormalization of the conduction band energy, a result of the mainly Pb-derived p level splitting into $p_{1/2}$ and $p_{3/2}$ states (see Table 1 and Fig. S1). The bandgap remains direct but decreases in magnitude by circa 0.8 eV.

The centre of inversion present in the orthorhombic phase of $\text{CH}_3\text{NH}_3\text{PbI}_3$ is lost in static representations of the tetragonal and cubic phases. There is now a shift of the band extrema away from the high-symmetry points: spin splitting is activated. The indirect bandgaps are 2.00 eV and 1.87 eV for the tetragonal and pseudocubic phases, and conduction-band minima are offset by 0.03 \AA^{-1} and 0.06 \AA^{-1} from high symmetry points. The latter calculated value is a giant spin splitting, comparable in magnitude to the largest values experimentally observed in bulk systems [38]. These band splitting features are consistent with the electron-hole recombination kinetics observed in experiment. In particular, there is a sharp fall off in the charge carrier lifetime at the transition to the orthorhombic phase, where a direct gap is recovered [22, 24].

The inversion-asymmetric tetragonal and pseudocubic structures have a Rashba-like spin splitting, with the usual k -linear dispersion relation and helical spin texture [14, 17, 18]. However, instead of a ring of extrema there are two distinct extremal points. These are antipodal to each other, with a connecting path that passes through two saddle points [13]. At the DFT level, the conduction and valence bands have approximately the same momentum offset Δk (difference in momentum between high-symmetry point and extremal point). However, QSGW results show that Δk in the valence band (VB) is roughly half that of the conduction band (CB). Relative to QSGW, LDA-DFT also tends to overestimate the energy offset ΔE (defined as the difference in energy between the spin-split extremal point and high-symmetry point) in both bands. Similar trends are seen for other cations, such as FAPbI₃ and CsPbI₃.

A central question is to what extent the calculated spin splitting depends on the choice of cation. The methylammonium cation has a large built-in dipole [42], which by itself applies a

local electric field to the lead-iodide octahedra. Another common organic cation, formamidinium ($\text{HC}(\text{NH}_2)_2$ or FA), possesses a much smaller dipole [42] but still breaks the inversion symmetry of the unit cell, and applies steric distortion to the octahedra (Fig. 1d). On the other hand, the inorganic cation in CsPbI_3 has spherical symmetry and there is no built-in dipole. The room-temperature phase is often assumed to be cubic (O_h point group), with a direct gap (see Fig. 1e).

We consider these cations in a range of structures (Table I with band structures in Fig. 1). Universally, once inversion symmetry is broken, a similar band splitting is observed. The cations do not directly affect the band splitting. Instead, they are found to play an indirect role by influencing the lead-iodide octahedral distortions through steric effects; it is the cage deformations that generate the spin splitting. In the case of the inorganic cesium, the ideal cubic structure has no spin splitting. If we substitute cesium for methylammonium in the pseudocubic structure, and energy minimise with respect to cesium while keeping Pb and I fixed, then an almost identical spin splitting is generated (see Fig. 1f).

In contrast to the average (long-range) cubic structure inferred from Bragg diffraction, recent measurements suggest that the structure of CsPbI_3 is locally symmetry broken at room temperature [43–45]. Polar fluctuations have recently been observed in a number of other perovskites [46]. Anticipating that thermal disorder in these soft materials is necessary to understand the size and nature of the spin splitting, we now consider finite-temperature effects.

Dynamic disorder at finite temperatures. Electronic structure calculations are typically athermal, the nuclear coordinates approximated as classical, definite, points in space. To consider finite temperature effects we sample structures from a thermodynamic ensemble. Within *ab initio* MD, the classical equations of motion for the nuclear coordinates are integrated with the forces from ground-state DFT calculations. The kinetic energy (temperature) of these ions is connected to a thermostat (chosen to be 300 K).

For the MD, we consider $2 \times 2 \times 2$ supercell expansions of the MAPbI_3 and CsPbI_3 unit cells, allowing for Brillouin zone boundary tilting modes. After an initial equilibration period, we sample 200 consecutive frames, each separated by 0.025 ps. This time discretisation is intentionally chosen to be less than the characteristic motion of the material (most particularly the 2 ps methylammonium rotation, and associated cage distortion). We can track the electronic structure and spin splitting evolve in time. For these snapshot structures, we calculate the electronic structure at the LDA level (all-electron with spin-orbit coupling). As discussed, we expect the momentum offset Δk to be in close agreement with QSGW for the CB, but largely overestimated in the VB.

For both materials the momentum offset Δk in the conduction band (Fig. 2) fluctuates around a value of 0.03 \AA^{-1} . A similar picture is seen for the energy offsets, with averages around 20 meV. In the valence band, larger differences in the average splittings are seen when comparing the two materials. The MA cation results in more variable behaviour, par-

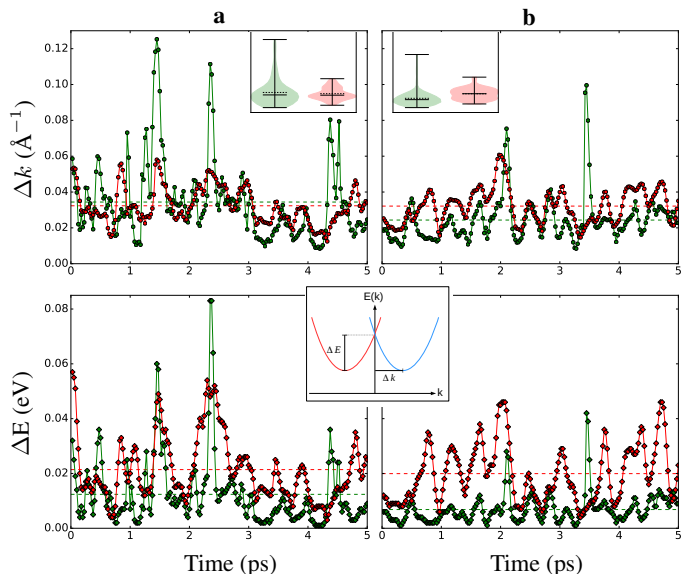


FIG. 2: Magnitude of momentum and energy offsets in the valence and conduction bands for (a) $\text{CH}_3\text{NH}_3\text{PbI}_3$ and (b) CsPbI_3 from 200 frames of *ab initio* molecular dynamics.

The valence band splittings are plotted in green and the conduction band splitting in red. The average splitting is plotted as dashed lines. The splitting schematic, using conduction band as example, highlights the spin splitting parameters ΔE and Δk . The probability densities of the momentum offsets are represented by inset violin plots, where the mean and median values are shown as dashed and solid lines.

ticularly in the VB, as evidenced by the larger spread (and broader distribution) in the inset violin plots. This is in line with the dominant contributions to the valence band coming from the lighter iodine atoms. Interestingly, the Cs cation, despite having the same average, results in a broader distribution in the conduction band. The splittings are reduced relative to the single cells but, crucially, are non-zero throughout.

As well as Δk changing in magnitude, the band extrema rotate relative to one another. The average angle between the line connecting the pair of minima in the conduction band and the line connecting the pair of maxima in the valence band is 44° for MAPbI_3 and 38° for CsPbI_3 (relative angles are as high as 90°). A plot of the angular dependence (Fig. S2), a scatter plot of the extremal point positions (Fig. S3), and a discussion of the sensitivity of the results can be found in the Supplemental Material.

The similar band splittings observed for both cesium and methylammonium suggest that the dominant contribution is thermal distortion of the inorganic cage. A Fourier transform of the time-series suggests the spin splitting has the same periodicity as low frequency phonon modes (Fig. S4). These modes are distortions of the octahedral cage and associated rotations of the organic cation in the case of MAPbI_3 . As such, spin splitting is expected to be present at room tempera-

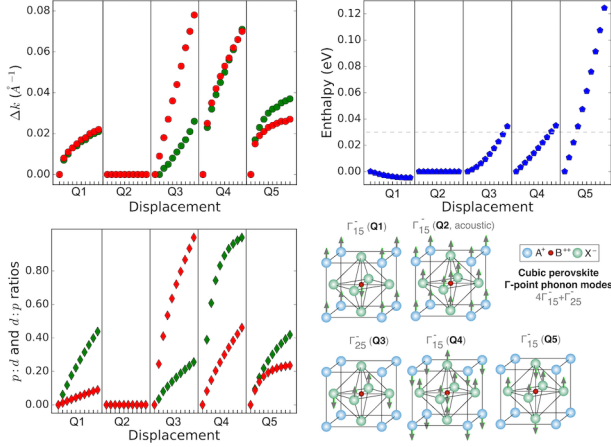


FIG. 3: Analysis of the five zone-centre phonon modes for cubic CsPbI₃. The effect of displacement along each mode (Q) is shown for: momentum offsets (Δk) in the valence (green) and conduction (red) bands; enthalpy change relative to reference cubic structure ($k_B T$ at 300 K is plotted as a dashed grey line); ratio of d : p -character (green) in the valence band maximum and p : d -character (red) in the conduction band minimum eigenstates versus displacement. The ratios are computed from Mulliken populations and both sets are normalised for comparison.

ture for all lead iodide based perovskites, largely independent of cation or (long-range) crystal symmetry.

CsPbI₃ is a striking example of the importance of finite temperature lattice dynamics on the electronic structure. A static calculation predicts no spin splitting. Such a cubic unit cell agrees with the average structure determined from X-ray diffraction [47]; however, this phase has a number of vibrational instabilities that give rise to dynamic distortions [48]. At any point in time, the lattice distortions break the local symmetry, give rise to local fields, and produce spin splitting. To better understand the structural origins of the splitting, we return to a (single) unit cell representation and follow symmetry breaking by phonon modes. In the frozen-phonon approximation, we separately distort along each of the Γ -point normal modes and track Δk . The magnitude of these distortions are chosen (from the phonon frequency) to sample a thermodynamic degree of freedom to an energy of $k_B T$ (300 K).

The five unique cubic-perovskite phonon modes are depicted in Fig. 3. The acoustic mode (Q2), is a rigid translation of the lattice and does not change the energy or electronic structure; it is included as a cross-validation. Each other mode results in a monotonic spin splitting as a function of displacement. The first mode is soft, corresponding to ‘rattling’ of the Cs and Pb ions. The dependence of Δk on displacement has the same form for both VB and CB. Notable differences in Δk are observed in both bands for Q3 and Q5. The largest initial (low displacement, low energy) splitting is observed for Q4, which corresponds to the Pb atom moving off site. Mode Q3 shows remarkably linear splitting as a function of disor-

tion. The mode is composed of octahedral twisting (iodine motion) around Pb. There are considerably larger splittings in the conduction band than in the valence band. The highest energy modes result in the largest splittings over the thermally accessible range.

Spin-orbit coupling is commonly considered a local effect, significant around heavy atoms. Here, the conduction band is primarily Pb- p orbital character and the valence band is primarily I- p character. Spin-orbit coupling is large close to the Pb ($Z=82$) and I ($Z=53$) nuclei. The spin splitting has its origins in spin-orbit coupling, which appears in the non-relativistic limit of the Dirac equation. The contribution to the electronic energy levels is the expectation value of the following spin-orbit correction to the scalar relativistic Hamiltonian:

$$H_{SOC} = \frac{2}{c^2} (\nabla V \times \mathbf{p}) \cdot \mathbf{s}$$

where V is the crystal potential, \mathbf{p} is a momentum operator, \mathbf{s} is a spin operator and c is the speed of light. Spin splitting is a result of local asymmetry in both the potential and the wavefunction (through the momentum operator) in the core regions of heavy nuclei; a large splitting requires a large value for both [49].

Previous work has shown that the asymmetry of the wavefunction strongly influences the magnitude of the spin splitting [49–51]. This can be estimated by the ratio of the l to $l \pm 1$ angular-momentum character in a region close to the nuclear core. The Mulliken populations in Fig. 3 do not project out small regions close to the nuclei; nevertheless, the ratios correlate closely to the observed shifts in Δk . There is a dependence on the choice of l - to $l \pm 1$ -character, with some trends, for example, better reproduced by the ratio of p : s (see Fig. S5). The spin splitting is also found to depend on local electric fields (see Fig. S6). These are spherical averages around the Pb and I locations (for iodine a vector average is taken). The angle between the electric field and the momentum offset vectors is approximately $90 \pm 2^\circ$ in each case, in line with the perpendicular relation between the electric field and momentum vectors in the Rashba model. The local symmetry breaking, resulting in asymmetry of both the potential and wavefunction, can be seen through changes in the charge density (contour plots are provided in Fig. S7).

To quantify the correlation for disordered structures, we calculate these measures (at the DFT level) for 147 random methylammonium orientations in a pseudocubic unit cell. The MA orientation is randomly sampled and the PbI₃ network is then locally relaxed around each configuration. Optimized structures with energy $> k_B T$ were excluded. The d : p and p : d ratios are found to correlate well with the magnitude of the momentum offset Δk (see Fig. 4). Improved agreement is expected by accounting for different l to $l \pm 1$ ratios [52] and by limiting the projections to regions close to the nuclear cores.

In addition to band splitting, structural distortions generally widen the bandgap and flatten the frontier bands. QSGW *underestimates* the bandgap in CsPbI₃ in the cubic struc-

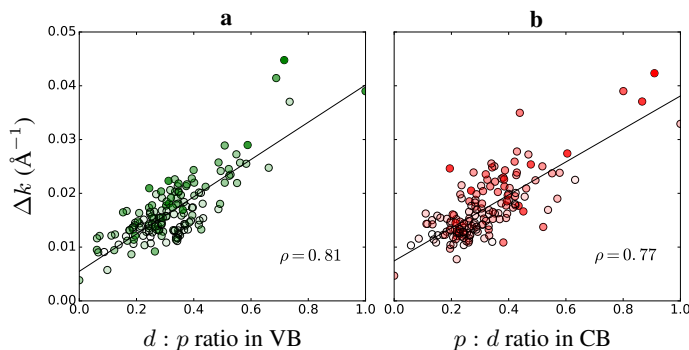


FIG. 4: Magnitude of momentum offset Δk versus (a) $d : p$ ratio in the VB and (b) $p : d$ ratio in the conduction band for 147 stochastically sampled MA orientations in MAPbI₃. The total energy of each structure is represented by the opacity level of the marker face colour, where higher opacity refers to higher energy. The Pearson correlation coefficient (ρ) between the splitting and ratio magnitudes is shown in the bottom right corner of the plots.

ture, while almost universally it slightly *overestimates* gaps in semiconductors and insulators [53]. However, QSGW predicts an increase of 0.44 eV in the pseudocubic structure relative to the cubic one (Table 1), improving agreement with room temperature experiments. Average MAPbI₃ and CsPbI₃ bandgaps from MD simulations also increase by 0.25 and 0.73 eV relative to athermal structures, and they increase for all displacements along the four CsPbI₃ optical phonon modes (See Fig. S8). These trends originate from two main sources: (1) the antibonding character of the frontier bands [54] and (2) a reduction in spin-orbit splitting of the CB originating from a reduction in Pb- p content. Both trends are demonstrated through an analysis of the shifts in the band edges with displacements along the normal modes. There is a general tendency for the valence band to be pushed *down* and for the conduction band to be pushed *up*, though how each edge shifts depends on the normal mode (see Fig. S8). The downshift of the valence band is in line with a reduction in antibonding between I- p and Pb- s states [54]. On the other hand, the CB upshift correlates closely with a reduction in Pb- p character and is largely a result of the reduced SO coupling of the state (see Fig. S9).

In summary, a spin-split indirect gap has been found in thermal ensembles of organic-inorganic and inorganic lead halide perovskites. The splitting arises due to relativistic spin-orbit coupling in the presence of local asymmetry, which we relate to distortions in the lead iodide framework. The role of the perovskite A-site cation appears to be steric in nature. By studying the effect of distortions along individual phonon modes, we uncover a mostly linear relationship between the energy of a distortion and the momentum offset. The asymmetry in the electronic wavefunction and, to a lesser extent, the local electric field were found to correlate well with the magnitude of the momentum offset. Overall, structural distortions

lead to spin-split bands and a widening of the bandgap. This provides a method to go from an observed (temperature-dependent) disorder measure to a measure of the indirect gap. Temperature-dependent observations of the band character for both the organic and inorganic perovskites will provide information to confirm these hypotheses.

In addition to the data in the Supplemental Material, a collection of input and output files, including crystal structures, are available in an on-line repository [DOI inserted upon acceptance].

Support has been received from the EPSRC (projects EP/M009580/1, EP/M011631/1 and EP/K016288/1). Via our membership of the UK's HEC Materials Chemistry Consortium, which is funded by EPSRC (EP/L000202), this work used the ARCHER UK National Supercomputing Service (<http://www.archer.ac.uk>).

* a.walsh@imperial.ac.uk

- [1] R. Elliott, Phys. Rev. **96**, 280 (1954).
- [2] R. Winkler, *Spin-orbit coupling effects in two-dimensional electron and hole systems* (Springer, 2003).
- [3] G. Dresselhaus, Phys. Rev. **100**, 580 (1955).
- [4] E. Rashba, Sov. Phys. Sol. State **1**, 368 (1959).
- [5] E. Rashba and V. Sheka, Fiz. Tverd. Tela **2**, 162 (1959).
- [6] E. I. Rashba, Soviet Physics-Solid State **2**, 1224 (1960).
- [7] G. Bihlmayer, O. Rader, and R. Winkler, New J. Phys. **17**, 050202 (2015).
- [8] Y. A. Bychkov and E. Rashba, JETP Lett. **39**, 78 (1984).
- [9] R. Winkler, Phys. Rev. B **69**, 045317 (2004).
- [10] X. Zhang, Q. Liu, J.-W. Luo, A. J. Freeman, and A. Zunger, Nature Phys. **10**, 387 (2014).
- [11] I. Žutić, J. Fabian, and S. D. Sarma, Rev. Mod. Phys. **76**, 323 (2004).
- [12] J. Fabian, A. Matos-Abiad, C. Ertler, P. Stano, and I. Zutic, arXiv:0711.1461 (2007).
- [13] F. Brivio, K. T. Butler, A. Walsh, and M. Van Schilfgaarde, Phys. Rev. B **89**, 155204 (2014).
- [14] M. Kim, J. Im, A. J. Freeman, J. Ihm, and H. Jin, P.N.A.S. **111**, 6900 (2014).
- [15] A. Amat, E. Mosconi, E. Ronca, C. Quarti, P. Umari, M. K. Nazeeruddin, M. Gratzel, and F. De Angelis, Nano Lett. **14**, 3608 (2014).
- [16] C. Motta, F. El-Mellouhi, S. Kais, N. Tabet, F. Alharbi, and S. Sanvito, Nature Comm. **6** (2015).
- [17] M. Kepenekian, R. Robles, C. Katan, D. Saporì, L. Pedesseau, and J. Even, ACS Nano **9**, 11557 (2015).
- [18] F. Zheng, L. Z. Tan, S. Liu, and A. M. Rappe, Nano Lett. **15**, 7794 (2015).
- [19] T. Etienne, E. Mosconi, and F. De Angelis, J. Phys. Chem. Lett. **7**, 1638 (2016).
- [20] E. Mosconi, T. Etienne, and F. De Angelis, J. Phys. Chem. Lett. **8**, 2247 (2017).
- [21] L. Z. Tan and A. M. Rappe, arXiv:1708.05436 (2017).
- [22] E. M. Hutter, M. C. Glvez-Rueda, A. Osherov, V. Bulovi, F. C. Grozema, S. D. Stranks, and T. J. Savenije, Nature Mater. **16**, 115 (2017).

- [23] D. Niesner, M. Wilhelm, I. Levchuk, A. Osvet, S. Shrestha, M. Batentschuk, C. Brabec, and T. Fauster, *Phys. Rev. Lett.* **117**, 126401 (2016).
- [24] T. Wang, B. Daiber, J. M. Frost, S. A. Mann, E. C. Garnett, A. Walsh, and B. Ehrler, *Energy Environ. Sci.* **10**, 509 (2017).
- [25] D. Niesner, M. Hauck, S. Shrestha, I. Levchuk, G. J. Matt, A. Osvet, M. Batentschuk, C. Brabec, H. B. Weber, and T. Fauster, *arXiv:1703.08740* (2017).
- [26] W. S. Yang, B.-W. Park, E. H. Jung, N. J. Jeon, Y. C. Kim, D. U. Lee, S. S. Shin, J. Seo, E. K. Kim, J. H. Noh, and S. I. Seok, *Science* **356**, 1376 (2017).
- [27] A. Kojima, K. Teshima, Y. Shirai, and T. Miyasaka, *Journal of the American Chemical Society* **131**, 6050 (2009).
- [28] T. M. Brenner, D. A. Egger, L. Kronik, G. Hodes, and D. Cahen, *Nature Rev. Mater.* **1**, 15007 (2016).
- [29] M. Ahmadi, T. Wu, and B. Hu, *Advanced Mater.* (2017).
- [30] P. Azarhoosh, S. McKechnie, J. M. Frost, A. Walsh, and M. Van Schilfgaarde, *APL Mater.* **4**, 091501 (2016).
- [31] L. D. Whalley, J. M. Frost, Y.-K. Jung, and A. Walsh, *J. Chem. Phys.* **146**, 220901 (2017).
- [32] J. Even, L. Pedesseau, J.-M. Jancu, and C. Katan, *J. Phys. Chem. Lett.* **4**, 2999 (2013).
- [33] P. Umari, E. Mosconi, and F. De Angelis, *Sci. Rep.* **4**, 4467 (2014).
- [34] M. R. Filip and F. Giustino, *Phys. Rev. B* **90**, 245145 (2014).
- [35] <http://www.questaal.org>. Our *GW* implementation was adapted from the original ecalj package, now at <https://github.com/tkotani/ecalj/>.
- [36] W. Kohn and L. J. Sham, *Phys. Rev.* **140**, A1133 (1965).
- [37] F. Brivio, J. M. Frost, J. M. Skelton, A. J. Jackson, O. J. Weber, M. T. Weller, A. R. Goni, A. M. Leguy, P. R. Barnes, and A. Walsh, *Phys. Rev. B* **92**, 144308 (2015).
- [38] K. Ishizaka, M. Bahramy, H. Murakawa, M. Sakano, T. Shimojima, T. Sonobe, K. Koizumi, S. Shin, H. Miyahara, A. Kimura, *et al.*, *Nature Mat.* **10**, 521 (2011).
- [39] K. Galkowski, A. Mitioglu, A. Miyata, P. Plochocka, O. Portugall, G. E. Eperon, J. T.-W. Wang, T. Stergiopoulos, S. D. Stranks, H. J. Snaith, *et al.*, *Energy Environ. Sci.* **9**, 962 (2016).
- [40] C. Quarti, E. Mosconi, J. M. Ball, V. D’Innocenzo, C. Tao, S. Pathak, H. J. Snaith, A. Petrozza, and F. De Angelis, *Energy Environ. Sci.* **9**, 155 (2016).
- [41] G. E. Eperon, G. M. Paternò, R. J. Sutton, A. Zampetti, A. A. Haghighirad, F. Cacialli, and H. J. Snaith, *J. Mater. Chem. A* **3**, 19688 (2015).
- [42] J. M. Frost, K. T. Butler, F. Brivio, C. H. Hendon, M. Van Schilfgaarde, and A. Walsh, *Nano Lett.* **14**, 2584 (2014).
- [43] F. Bertolotti, L. Protesescu, M. V. Kovalenko, S. Yakunin, A. Cervellino, S. J. Billinge, M. W. Terban, J. S. Pedersen, N. Masciocchi, and A. Guagliardi, *ACS nano* **11**, 3819 (2017).
- [44] O. Yaffe, Y. Guo, L. Z. Tan, D. A. Egger, T. Hull, C. C. Stoumpos, F. Zheng, T. F. Heinz, L. Kronik, M. G. Kanatzidis, J. S. Owen, A. M. Rappe, M. A. Pimenta, and L. E. Brus, *Phys. Rev. Lett.* **118**, 136001 (2017).
- [45] M. Isarov, L. Z. Tan, M. I. Bodnarchuk, M. V. Kovalenko, A. M. Rappe, and E. Lifshitz, *Nano Lett.* **17**, 5020 (2017).
- [46] P. Guo, Y. Xia, J. Gong, C. C. Stoumpos, K. M. McCall, G. C. Alexander, Z. Ma, H. Zhou, D. J. Gosztola, J. B. Ketterson, *et al.*, *ACS Energy Lett.* **2**, 2463 (2017).
- [47] C. K. Møller, *Nature* **182**, 1436 (1958).
- [48] R. X. Yang, J. M. Skelton, L. da Silva, J. M. Frost, and A. Walsh, *J. Phys. Chem. Lett.* **8**, 4720 (2017).
- [49] G. Bihlmayer, Y. M. Koroteev, P. Echenique, E. Chulkov, and S. Blügel, *Surface Sci.* **600**, 3888 (2006).
- [50] M. Nagano, A. Kodama, T. Shishidou, and T. Oguchi, *J. Phys.: Cond. Matter* **21**, 064239 (2009).
- [51] S. Abdelouahed and J. Henk, *Phys. Rev. B* **82**, 193411 (2010).
- [52] For instance, Pearson correlation coefficient values are as high as 0.94 in the valence band for $p : s$ and $p : d$ ratios based on projections for iodine alone.
- [53] M. van Schilfgaarde, T. Kotani, and S. Faleev, *Phys. Rev. Lett.* **96**, 226402 (2006).
- [54] L.-Y. Huang and W. R. Lambrecht, *Phys. Rev. B* **88**, 165203 (2013).
- [55] in *Electronic Structure and Physical Properties of Solids*, edited by H. Dreyssé (Springer, Berlin, 2000) p. 114.
- [56] M. van Schilfgaarde, T. Kotani, and S. V. Faleev, *Phys. Rev. B* **74**, 245125 (2006).
- [57] H. Ebert, *J. Phys.: Cond. Matter* **1**, 9111 (1989).
- [58] A. M. A. Leguy, A. R. Goni, J. M. Frost, J. Skelton, F. Brivio, X. Rodríguez-Martínez, O. J. Weber, A. Pallipurath, M. I. Alonso, M. Campoy-Quiles, M. T. Weller, J. Nelson, A. Walsh, and P. R. F. Barnes, *Phys. Chem. Chem. Phys.* **18**, 27051 (2016).

Supplemental Material for ‘Dynamic Symmetry Breaking and Spin Splitting in Metal Halide Perovskites’

ADDITIONAL COMPUTATIONAL DETAILS

Electronic structure calculations are carried out using the full-potential linearized muffin-tin orbital (FP-LMTO) method [55, 56] as implemented in the QUESTAAL code [35]. All results presented use either the local density approximation (LDA) [36] or the quasiparticle self-consistent GW (QSGW) method [53], using the LDA as the starting point. The basis set consists of two smoothed Hankel envelope functions per l channel and local orbitals are included for Pb (5*d*), Cs (5*s*) and I (high-lying *s* and *p*). Additional ‘floating orbitals’ up to $l = 1$ are also included to provide a better description of the interstitial regions. $6 \times 6 \times 6$ and $4 \times 4 \times 4$ k -point meshes are used for single cell and supercell DFT calculations respectively. A $4 \times 4 \times 4$ k -point mesh is used in the QSGW calculations. The QSGW bandgaps were found to be sensitive to the product basis tolerance and more conservative settings were used. Free atom calculations (see Table S1) are carried out using both scalar Dirac and fully relativistic Dirac formulations [57].

A key finding in our work is that the magnitude of the spin-split momentum offset is sensitive to the structure. Our ab-initio molecular dynamics is conducted with the VASP codes. This is a plane-wave code that makes use of pseudo-potentials. A key necessity is to use pseudopotentials (i.e. Pb_d) which treat the d-electrons explicitly, in order to get a correct representation of the dynamic bonding environment and crystal field of the lead ion.

In our prior work [30], we briefly studied samples from ab-initio molecular dynamics on $2 \times 2 \times 2$ unit cell with Γ -point sampling and a small basis set (300 eV cutoff). It is generally expected that using such underconserved values in a plane wave code has the effect of softening the potential energy landscape, leading to an artificially higher effective temperature (greater thermal fluctuations). After tests, we found that the lead thermal displacements were uniquely sensitive to the reciprocal space sampling. Using a $3 \times 3 \times 3$ k -point integration, we find reduced structural distortions and splittings, compared to our earlier work.

Representative single-unit cells with randomised methylammonium orientation were generated in a stochastic manner. This followed a prescription we had developed for and applied to stochastic sampling of the phonon spectrum[58]. Starting with an optimised pseudo-cubic structure, the methylammonium was removed, and then randomly reorientated by applying a rotation matrix generated from a quaternion populated with pseudo-random normally distributed values. A normally distributed shift (standard deviation of 0.05 lattice vectors) was also applied to the methylammonium to further randomise the starting configuration. 101 steps of conjugate gradient optimisation of the ionic locations were then applied to these structures, with the PBEsol functional and a 700 eV cutoff in the kinetic energy. This local optimisation procedure first fixes the ‘bad contacts’ between overlapping atoms, but due to the local nature ends up in a local representative minima. The resulting structures were extracted, along with the final DFT total energy. This produced 249 unique structures.

The DFT total energies were then assessed. A partition function was calculated by summing over the sampled DFT energies. Examples with a thermodynamic probability of $p < 1e^{-5}$ compared to the lowest energy structure were discarded. At our chosen temperature $T = 300$ K, this is an energy cutoff of 297.6 meV. The result was an ensemble of 147 athermal structures, representative of a thermodynamic ensemble at 300 K.

	Atomic energy levels (eV)				
	Pb	I	N	C	H
<i>s</i>	-12.4	-17.73	-18.5	-13.73	-6.44
$s_{\frac{1}{2}}$	-12.31	-17.68	-18.5	-13.72	-6.44
<i>p</i>	-3.79	-7.33	-7.32	-5.5	
$p_{\frac{1}{2}}$	-4.87	-8.0	-7.33	-5.51	
$p_{\frac{3}{2}}$	-3.36	-6.97	-7.32	-5.5	
$p - p_{\frac{1}{2}}$	1.08	0.68	0.01	0.0	

TABLE S1: Relativistic atomic energy levels. The *s* and *p* refer to the standard scalar-relativistic energy levels (without SOC), while $s_{\frac{1}{2}}$, $p_{\frac{1}{2}}$ and $p_{\frac{3}{2}}$ are the fully-relativistic Dirac energy levels. The $p - p_{\frac{1}{2}}$ is a measure of the gap reduction as a result of relativistic effects.

	Effective masses	
	VB	CB
MAPbI ₃ orthorhombic	-0.17, -0.21, -0.22	0.22, 0.21, 0.13
MAPbI ₃ tetragonal	-0.81, -0.86, -2.82	26.17, 0.96, 0.55
MAPbI ₃ pseudocubic	-0.16, -0.31, -0.50	0.97, 0.17, 0.14
FAPbI ₃ pseudocubic	-0.11, -0.17, -0.23	0.15, 0.14, 0.12
CsPbI ₃ cubic	-0.12, -0.12, -0.12	0.12, 0.12, 0.12
CsPbI ₃ pseudocubic	-0.15, -0.16, -0.79	0.60, 0.18, 0.14
Mode 1	-0.03, -0.04, -2.54	2.03, 0.03, 0.03
Mode 2	-0.02, -0.02, -0.02	0.02, 0.02, 0.02
Mode 3	-0.16, -0.25, -0.43	0.18, 0.12, 0.12
Mode 4	-0.10, -0.17, -0.98	0.36, 0.11, 0.08
Mode 5	-0.07, -0.11, -1.26	1.32, 0.12, 0.06

TABLE S2: Valence and conduction band effective masses. The three components m_1 , m_2 , m_3 are the effective masses along the principal axes of an ellipsoidal fit. The first six rows show results from QSGW calculations. The following five rows contain LDA effective masses for CsPbI₃ cubic following the maximum (thermal) displacement along each of the five phonon modes. Note that Mode 2 (acoustic) corresponds to an undistorted cubic cell.

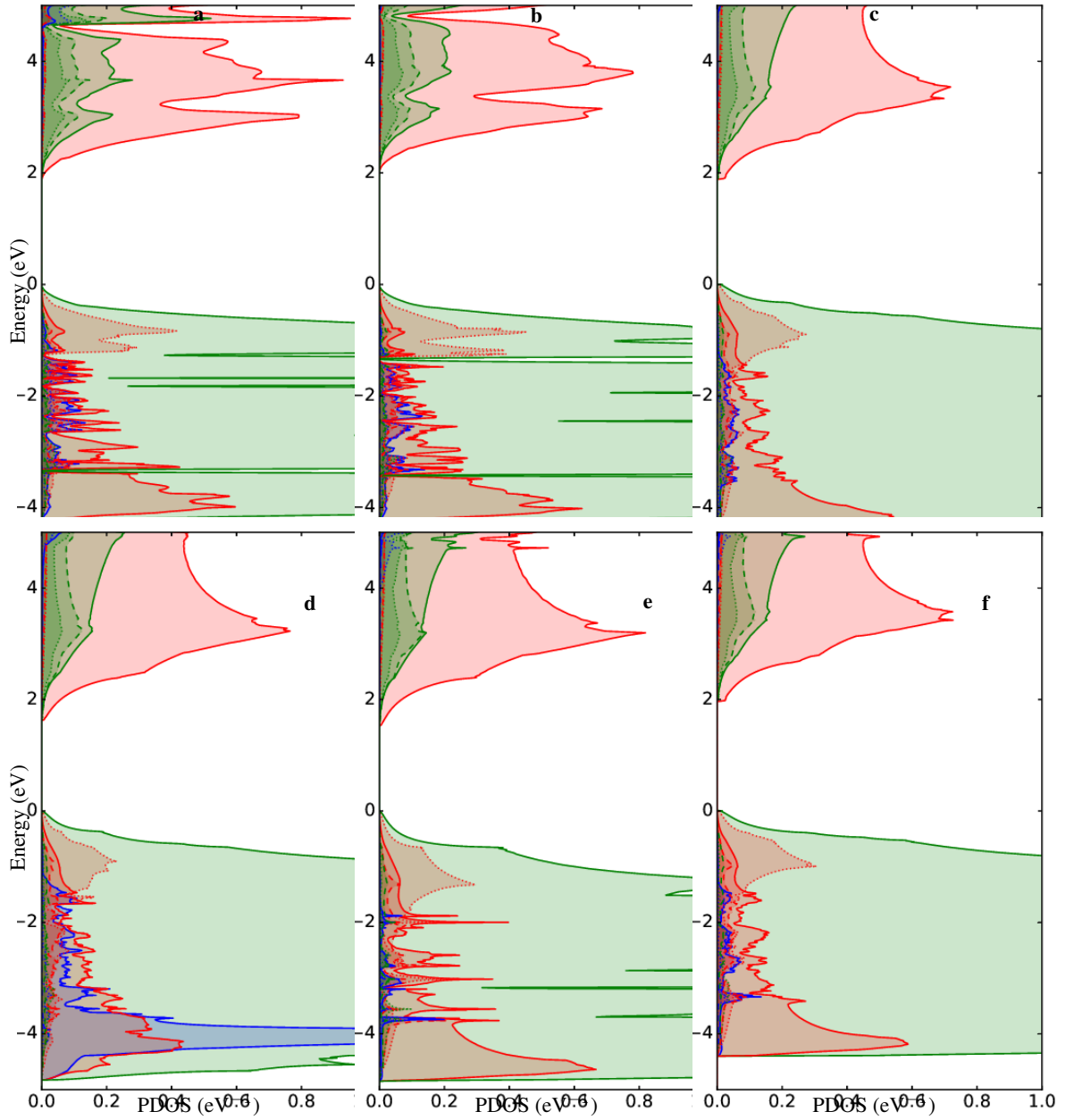


FIG. S1: Partial electronic density of states from QSGW calculations. The decomposition is based on a partial wave analysis (projection onto partial waves in augmentation spheres). Pb, I and cation (MA, FA or Cs) contributions are colored red, green and blue respectively. The s , p and d orbitals are denoted by dotted, solid and dashed lines. The first row, starting from the left, contains MAPbI₃ in its (a) orthorhombic, (b) tetragonal and (c) pseudocubic phases. The second row shows FAPbI₃ in a (d) pseudocubic structure and CsPbI₃ in (e) cubic and (f) pseudocubic structures. The pseudocubic CsPbI₃ is obtained by substituting Cs into MAPbI₃.

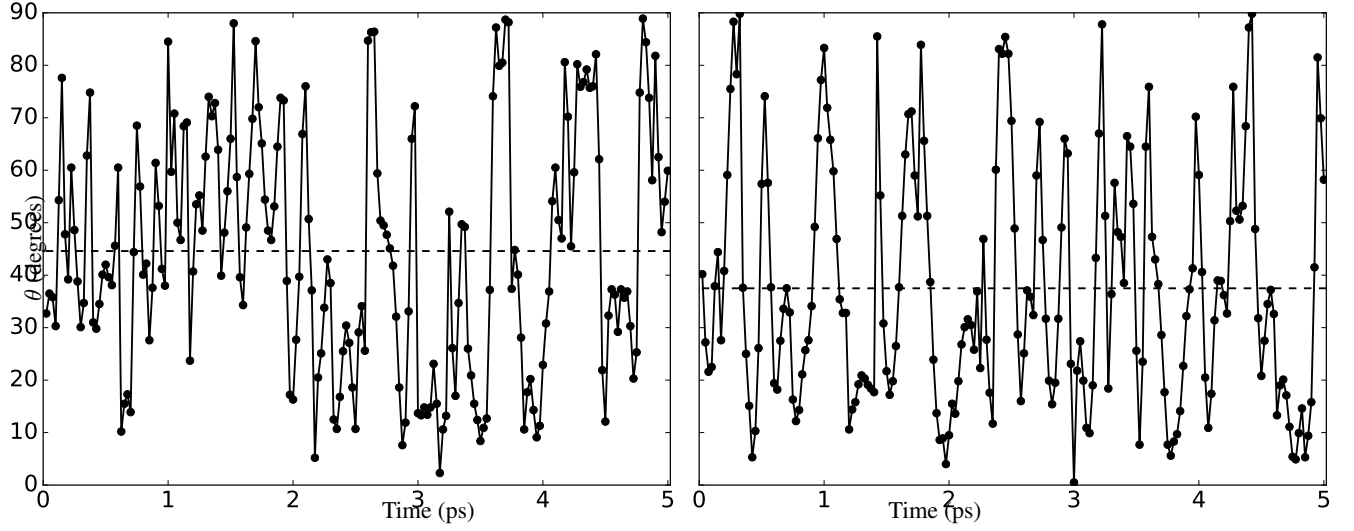


FIG. S2: Angle between momentum offsets in valence and conduction bands versus time. The angle is between the line connecting the pair of minima in the conduction band and line connecting the pair of maxima in the valence band. Average angles are shown as dashed lines.

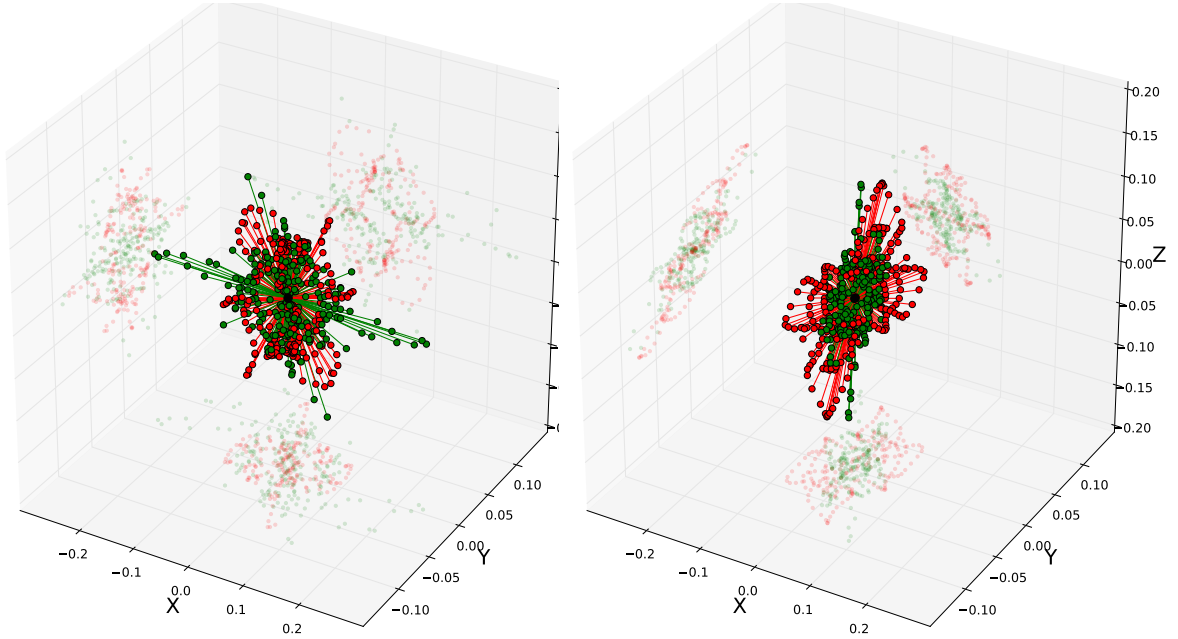


FIG. S3: Scatter plot of extremal point positions in MAPbI₃ (left) and CsPbI₃ (right) for 100 frames (first 2.5 ps of the 5 ps set). Four points and two lines are plotted from each frame: pair of maxima in the valence band (green), pair of minima in the conduction band (red) and lines connecting each extremal pair. Projections onto the x , y and z axes are also shown.

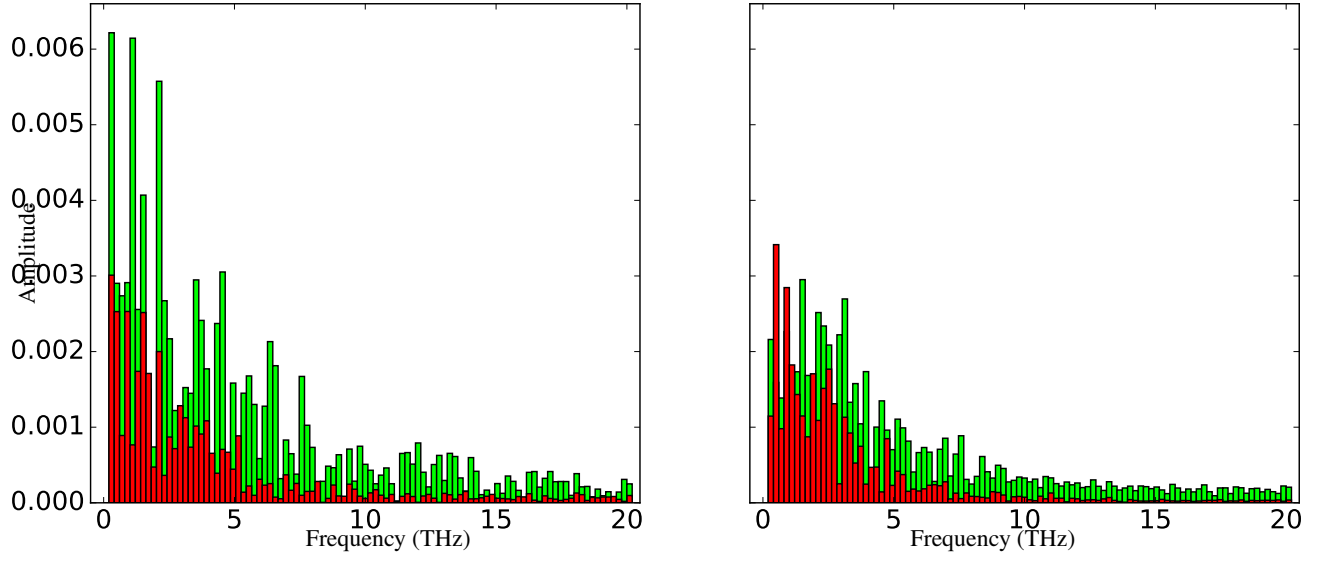


FIG. S4: Fourier transform of momentum-offset time series for MAPbI₃ (left) and CsPbI₃ (right). Fourier transforms are shown for valence (green) and conduction (red) band splittings.

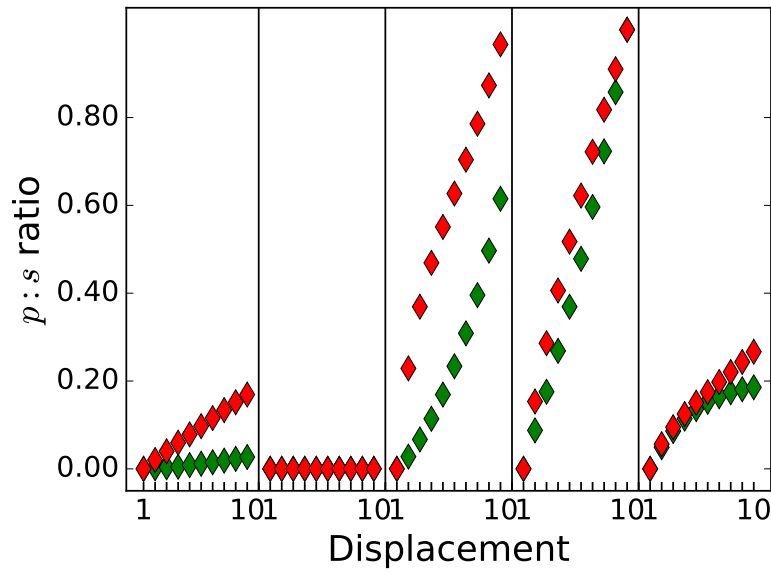


FIG. S5: Ratio of p : s -character (green) in the valence band maximum and p : s -character (red) in the conduction band minimum versus displacement along a normal mode.

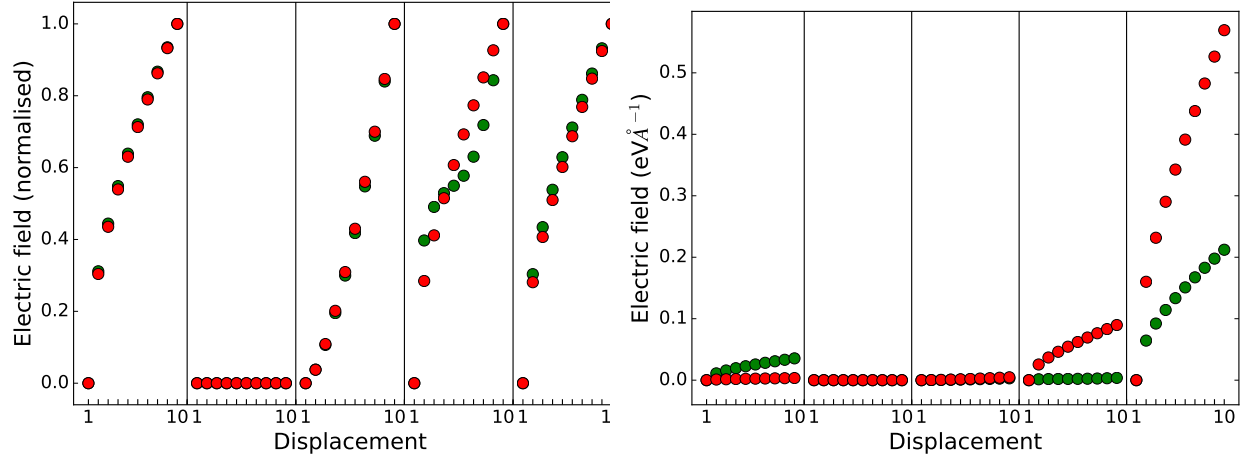


FIG. S6: Average electric field at the Pb site (red) and I sites (green) versus displacement along a normal mode. In the left handside plot, the fields have been normalised relative to the max and min in each mode. A vector average is taken over the three I sites. Unlike in the case of l character ratios, the relative magnitudes of the splittings are not well described across different modes.

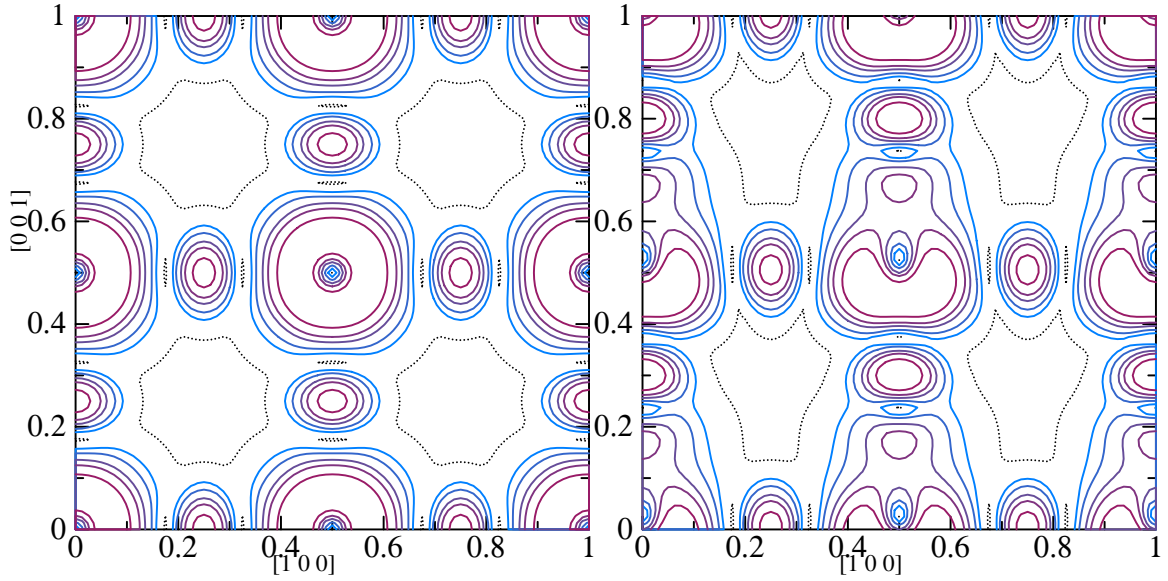


FIG. S7: Example charge density plots for the undistorted (left) and max distorted (right) structures from the fifth phonon mode. The charge density is evaluated for the conduction band minimum eigenstates (at the R point and spin-split point). A (010) or xz plane that passes through the Pb atom at the origin is shown. The cell has been doubled for better viewing, with the Pb atoms positioned at the corners and at the centre of the plot. In the distorted case, the electric field is predominantly along the z -axis and the momentum splitting is the the xy plane.

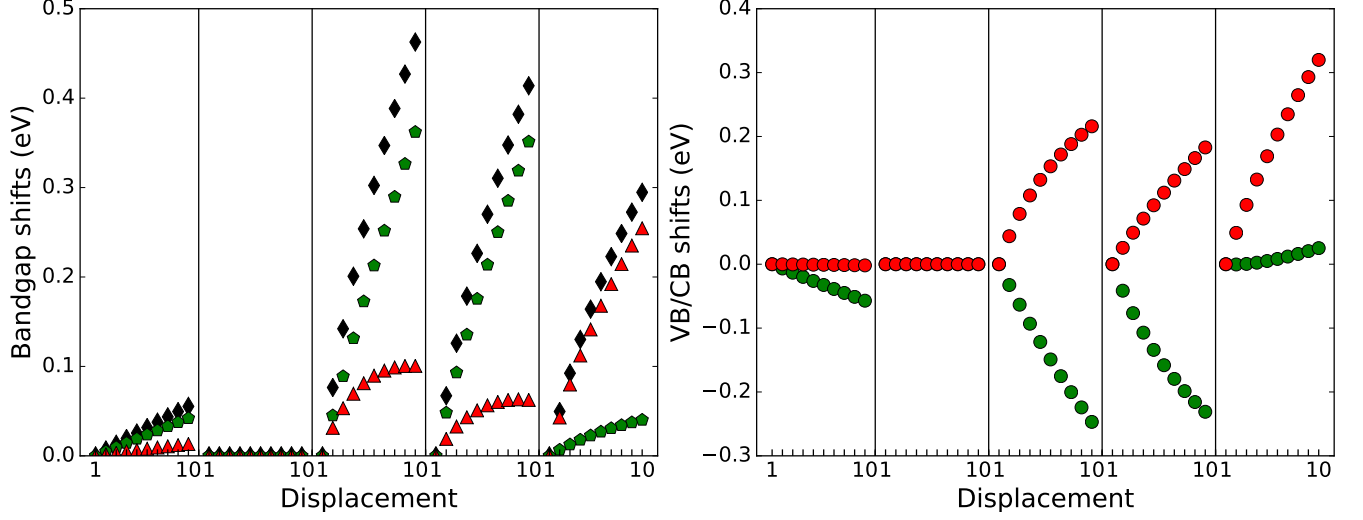


FIG. S8: Plot of bandgap energy changes versus displacement along a normal mode (left) and extremal point eigenvalue changes versus displacement along a normal mode (right). Both plots consider changes relative to the undistorted cubic structure. In the left handside plot, the total change with SOC is shown in black, change without SOC (scalar relativistic) is shown in green and change due to SOC (difference between total and scalar relativistic changes) is shown in red. In the right handside plot, the change in valence band maximum (VBM) is shown in green and change in conduction band minimum (CBM) is shown in red. To align the bands for different displacements, the average potential in the unit cell is kept fixed (see Figure S10 caption). Distortion is shown to widen the gap in all cases, with a rise in CBM eigenvalues and tends to lower the VBM eigenvalues. Interestingly, there is a small rise in the VBM energies for mode 5; possibly a result of increased antibonding for those displacements.

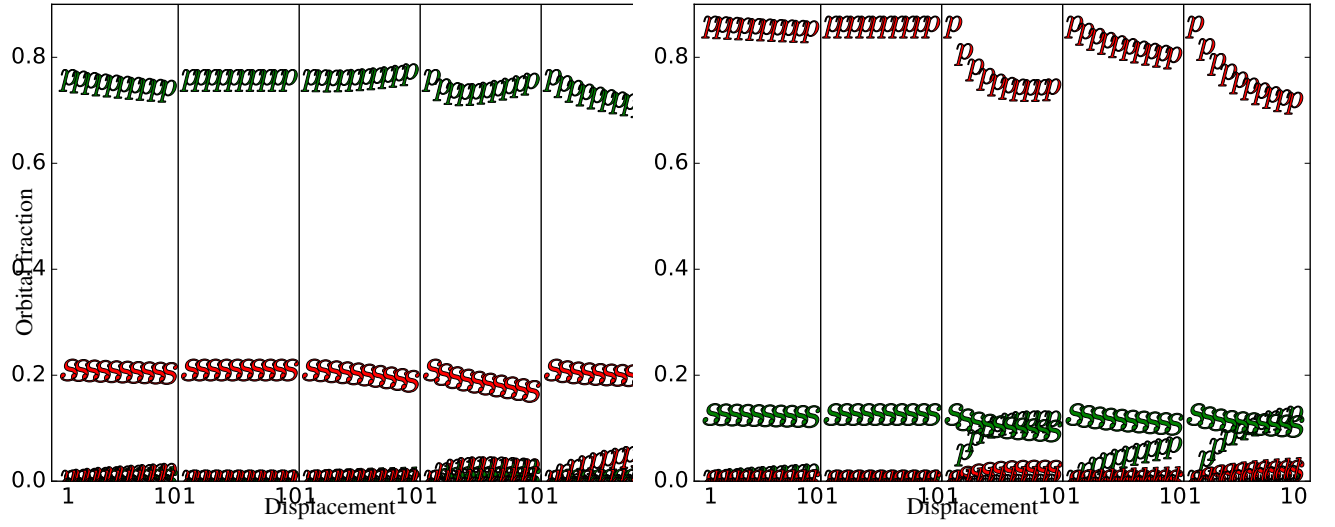


FIG. S9: Orbital-character fraction versus displacement for valence band maximum (left) and conduction band minimum (right) eigenstates. The decomposition is based on a Mulliken analysis, which conveniently provides percentage orbital contributions for a given eigenstate. However, unlike in the partial wave analysis, the inclusion of interstitial regions means there is an ambiguity in the choice of basis functions in regions of overlap; there is a dependence on the basis set. The Mulliken PDOS predicts a strong I- d character in the conduction band (right plot). However, the partial wave PDOS, which is more reliable, assigns these contributions to Pb- p states. To account for this, the I- d fraction is added to the Pb- p fraction. Nevertheless, the basis set is constant across distorted structures and so the trends are expected to be reliable. The Pb and I contributions are colored red and green, while the angular momentum character $l = 0$, $l = 1$ and $l = 2$ is represented by the markers s , p and d .

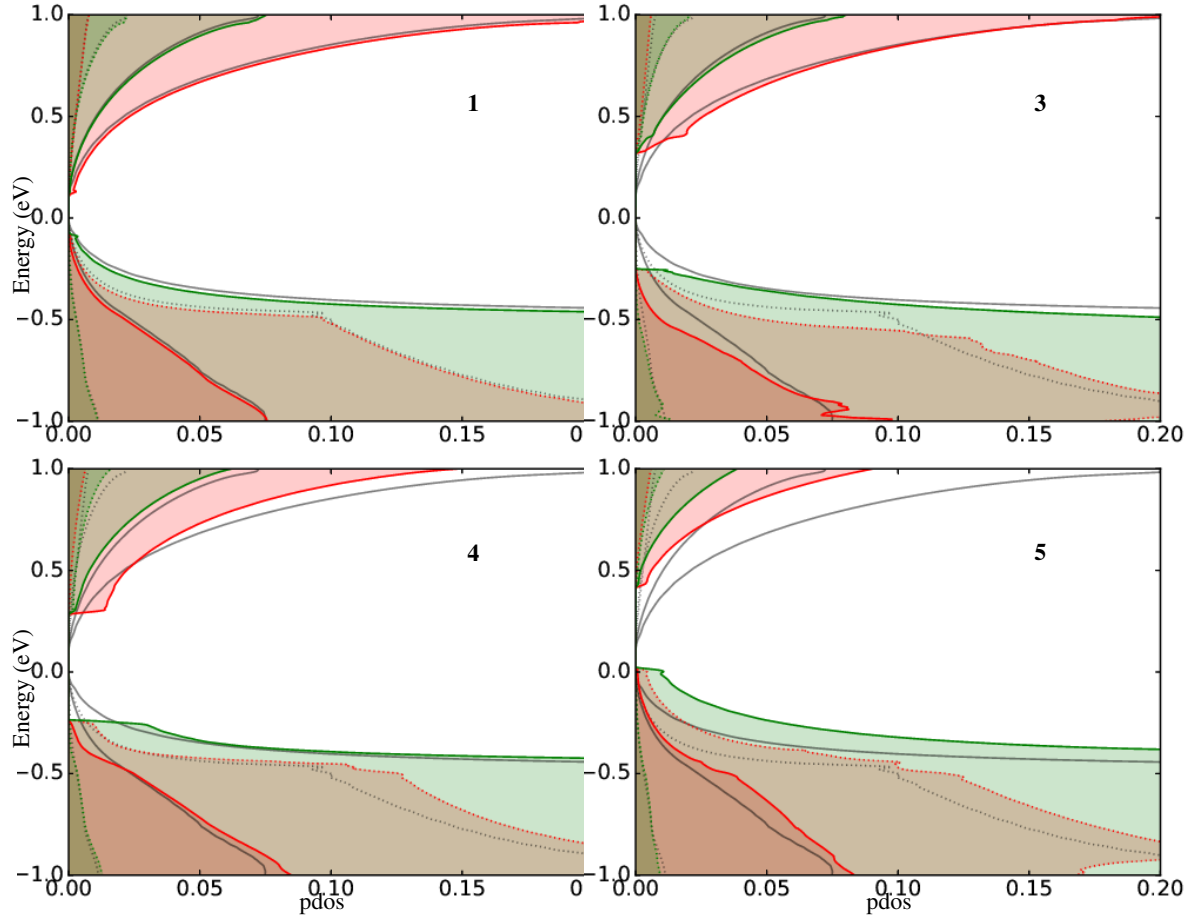


FIG. S10: LDA partial densities of states for maximum displacements along phonon modes 1, 3, 4 and 5. The PDOS for the reference cubic structure is shown in grey. To align the bands for different displacements, the average potential in the unit cell is kept fixed (this was found to be equivalent to alignment based on the onset of the valence I - p states).

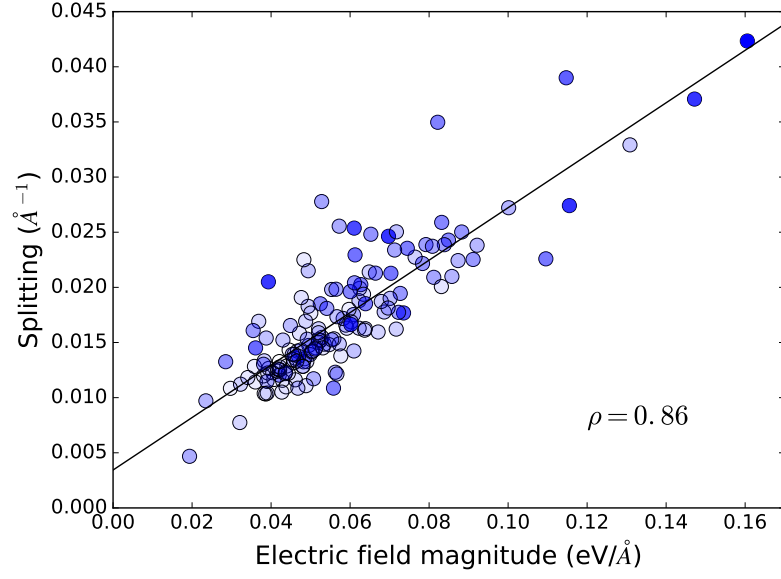


FIG. S11: Conduction band momentum offset plotted against the magnitude of the electric field at the Pb site for 147 stochastically sampled MA orientations in MAPbI_3 . The total energy of each structure is represented by the opacity level of the marker face colour, where higher opacity refers to higher energy. The Pearson correlation coefficient (ρ) between the splitting and electric field magnitudes is shown in the bottom right corner of the plot.